JOURNAL OF MATERIALS SCIENCE 17 (1982) 3253–3262

Thermal stability and crystallization behaviour of amorphous Zr–M–Si (M = IV–VIII group transition metals) alloys

A. INOUE, Y. TAKAHASHI*, C. SURYANARAYANA†, T. MASUMOTO
*The Research Institute for Iron, Steel and Other Metals, and *Graduate School, Tohoku University, Sendai 980, Japan*

By rapidly quenching with a melt-spinning apparatus, it has been possible to produce ductile amorphous single-phase ternary $Zr_{85-x}M_xSi_{15}$ (M = IV–VIII group transition metals) alloys in wide composition ranges. The crystallization temperature, activation energy for crystallization and hardness increase significantly only with the addition of group V and VI elements (V, Nb, Ta, Cr, Mo and W). Such a solute element effect could be interpreted on the basis that the chemical bonding between the solute elements and silicon is stronger for the group V and VI elements than for the other group elements. Crystallization studies of the amorphous $Zr_{85}Si_{15}$ and $Zr_{65}Nb_{20}Si_{15}$ alloys have been carried out through transmission electron microscopy and differential scanning calorimetry techniques. The binary alloy crystallizes by the uniform precipitation of b c c β-Zr over the entire area of the amorphous matrix followed by the appearance of the metastable b c tetragonal Zr_3Si compound from the remaining amorphous phase. On the other hand, the ternary alloy transforms by the simultaneous precipitation of β-Zr(Nb) and b c tetragonal Nb_3Si. The β-Zr and Zr_3Si phases were found to be in metastable states, the equilibrium structure being a mixture of α-Zr and Zr_4Si compound in the binary alloy.

1. Introduction

It is well known [1] that the metal–metal alloys consisting of zirconium and late transition metal such as Zr–Fe, Zr–Co, Zr–Ni, Zr–Cu and Zr–Pd form relatively easily an amorphous phase by the conventional melt-spinning technique. Consequently, the physical, chemical, mechanical and electronic properties of these amorphous alloys have been extensively studied from both the technological and fundamental points of view [2, 3]. In zirconium–metalloid alloys, on the other hand, there is hardly any information either on the amorphous phase-forming ability or on the properties, probably because of the difficulties involved due to their high melting temperatures and high reactivity with elements such as oxygen.

Recently, we have carried out a systematic study on the amorphous phase formation in zirconium–metalloid alloys such as Zr–(B, Al, C, Si, Ge, Sn) and Zr–M–(B, Al, C, Si, Ge, Sn) (M = IV–VIII group transition metals) by using a melt-spinning apparatus designed for refractory metal-based alloys and reported that the binary Zr–Si alloys form an amorphous phase exhibiting superconductivity as well as good mechanical properties [4–6]. The present paper deals with the amorphous phase formation range in Zr–M–Si systems and the crystallization temperature, activation energy for crystallization and crystallization behaviour of the amorphous alloys.

2. Experimental procedures

The specimens used in the present work are $Zr_{100-x}Si_x$ binary and $Zr_{85-x}M_xSi_{15}$ (M = Ti, Hf, V, Nb, Ta, Cr, Mo, W, Mn, Fe, Co, Ni or Cu) ternary alloys, where the subscripts represent

†Permanent address: Department of Metallurgical Engineering, Banaras Hindu University, Varanasi-221005, India.

0022–2461/82/113253–10$03.70/0

atomic percentages of the respective components. Mixtures of zirconium (99.6 wt%), pure metal M and silicon (99.999 wt%) were melted in an argon atmosphere using an arc furnace. The method of producing ribbon specimens of about 1 to 2 mm width and 0.02 to 0.03 mm thickness has previously been described elsewhere [4].

The as-quenched phases and their structural changes upon heating were characterized by conventional X-ray diffraction methods using nickel-filtered CuKα radiation and transmission electron microscopy. The transmission electron microscope samples were electrolytically thinned in an electrolyte consisting of 95 parts methanol and 5 parts sulphuric acid, the electrolyte being cooled to approximately 220 K. The crystallization temperature and the activation energy for crystallization were examined by a differential scanning calorimeter (DSC) at various heating rates ranging from 5 to 80 K min^{-1}. Hardness was measured with a Vickers microhardness tester using a 100 g load. The ductile–brittle nature of the as-quenched samples were tested in a simple bend test.

3. Results

3.1. Formation range of the amorphous phase

The composition range in which the homogeneous amorphous phase formed in the $Zr_{85-x}M_xSi_{15}$ ternary system is shown in Fig. 1. It can be seen that the amorphous phase forms in the wide composition range from 0 to 85 at% Ti or Hf, 0 to 80 at% Nb, 0 to 40 at% V or Ta and 0 to ~ 20 at% in the case of replacement of zirconium by chromium, molybdenum, tungsten, manganese, iron, cobalt, nickel or copper. Thus, the amorphous-phase formation range becomes wider in the order of chromium ≃ molybdenum ≃ tungsten ≃ manganese ≃ iron ≃ cobalt ≃ nickel ≃ copper < vanadium ≃ tantalum < niobium < titanium ≃ hafnium, in disagreement with the tendency [7, 8] of the amorphous-phase formation in zirconium–metal-type alloys. Furthermore, one can see in Fig. 1 that the $Ti_{85}Si_{15}$ [9] and $Hf_{85}Si_{15}$ [10] alloys also form an amorphous phase. This indicates that the dissolution of silicon significantly enhances the amorphous-phase-forming tendency of IVa transition metal (Ti, Zr, Hf)-based alloys and the effectiveness tends to decrease with increase in the group number of the solute elements. Bright-field electron micrographs and the corresponding diffraction patterns of the amorphous phase in the thinned $Zr_{65}V_{20}Si_{15}$ and $Zr_{65}Nb_{20}Si_{15}$ alloys are shown in Fig. 2. Lack of contrast in the micrographs (a and c) and the presence of diffuse halos in the diffraction patterns (b and d) testify the amorphous nature of the as-quenched alloys. Even at very high magnification, no evidence for the presence of crystalline inclusions was found by means of dark-field electron microscopy for the alloys within the composition ranges described above.

It has long been recognized [11–14] that the formation of the amorphous phase is closely related to the reduced glass temperature T_g/T_m (where T_g is the glass transition temperature and T_m is the melting temperature) and the viscosity of the alloys; that is, the larger the T_g/T_m and the higher the viscosity of the supercooled liquid, the greater is the ease of formation of the amorphous phase. It is worth mentioning in this connection that the composition range in which amorphous alloys are obtained by liquid-quenching techniques is in the vicinity of a deep eutectic in the corresponding phase diagram, where T_m is the lowest.

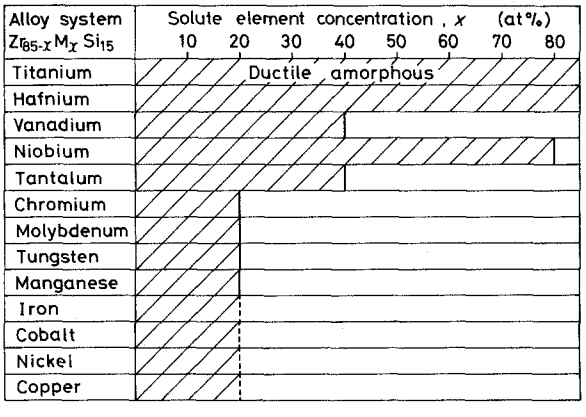

Figure 1 Composition range for the formation of the amorphous phase in ternary $Zr_{85-x}M_xSi_{15}$ alloys.

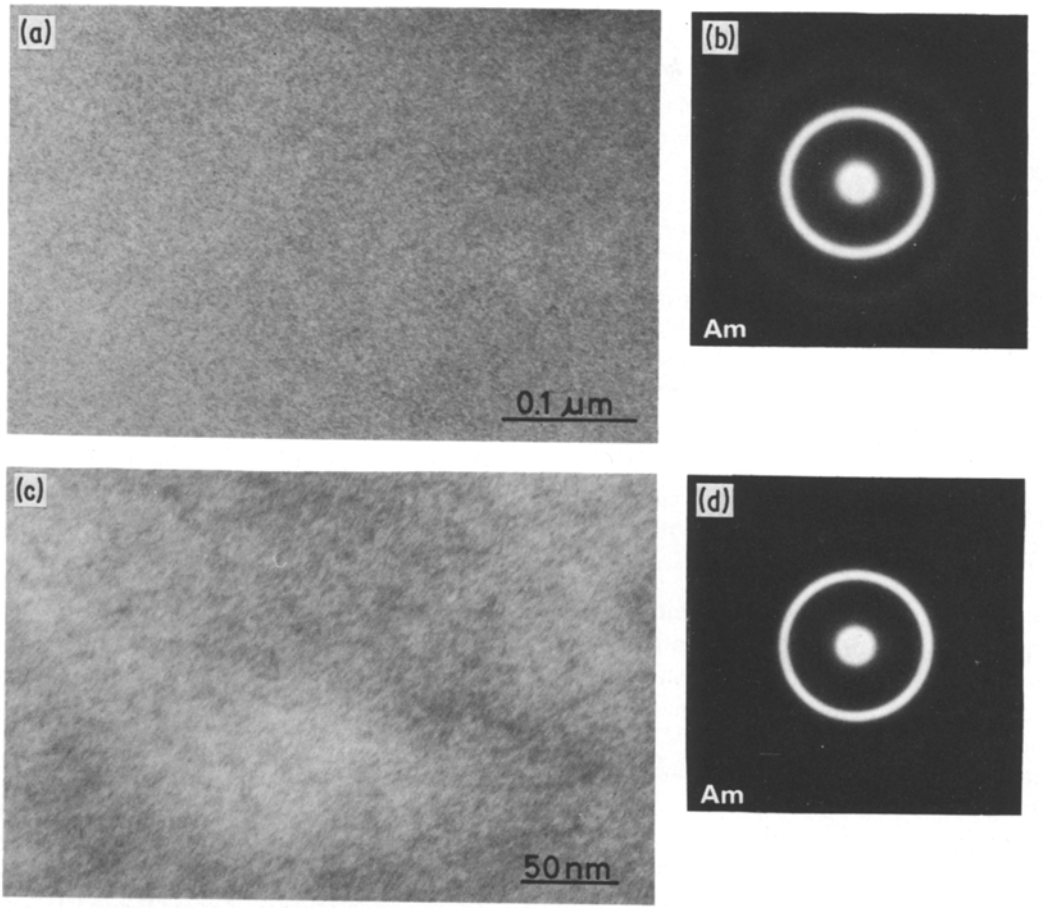

Figure 2 Bright-field electron micrographs and selected-area diffraction patterns showing the typical amorphous structure in the as-quenched $Zr_{65}V_{20}Si_{15}$ (a and b) and $Zr_{65}Nb_{20}Si_{15}$ (c and d) alloys.

Almost all the equilibrium diagrams for Zr–Si and M–Si binary alloys used in the present investigation exhibit a eutectic reaction at the Zr- and M-rich compositions [15]. The present amorphous phase-forming composition ranges appear to fall around the troughs of the eutectics in the Zr–M–Si ternary systems.

A similar behaviour was observed in Ti–M–Si (M ≒ IV–VIII group transition metals) and Hf-(V or Nb)-Si systems. The increased tendency to form amorphous phases in alloys having compositions near a deep eutectic has been interpreted in terms of a comparatively large negative heat of formation of the liquid alloy [16]. Furthermore, strong chemical interaction between zirconium and silicon and solute M metals and silicon is expected to yield significantly high values of T_g and viscosity, thus aiding in the formation of the amorphous phase. Finally, it may be both interesting and important to note that the formation range of $Zr_{85-x}M_xSi_{15}$ amorphous alloys becomes wider with increasing values of $(T_p - T_e)/X_e$ which corresponds to the slope of the liquidus line. Here T_p is the melting point of M, T_e is the eutectic temperature and X_e is the eutectic composition represented in atomic per cent.

3.2. Thermal stability and hardness

Fig. 3 shows the change in crystallization temperature (T_x) by the replacement of zirconium with solute element M in the $Zr_{85-x}M_xSi_{15}$ amorphous alloys. T_x was determined as the beginning point of the exothermic peak on the DSC curves measured at a heating rate of 20 K min^{-1}. The solute element effect can be divided into three groups: (1) the b c c elements tungsten, molybdenum, tantalum, chromium, vanadium and niobium which significantly enhance the T_x even with a small addition, (2) addition of iron, manganese, titanium and hafnium results only in a

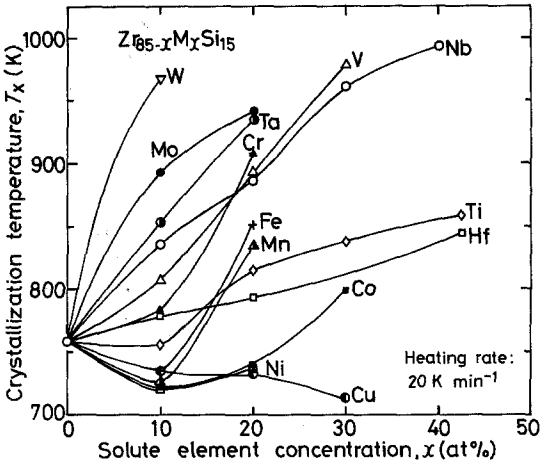

Figure 3 Change in the crystallization temperature (T_x) of $Zr_{85-x}M_xSi_{15}$ ternary amorphous alloys with solute element content.

slight increase in T_x even when present in substantial quantities, and (3) the f c c elements nickel and copper, decrease the T_x. This result indicates that the stability with respect to continuous heating enhances by the addition of group V and VI elements (V, Nb, Ta, Cr, Mo and W), having the b c c structure.

The effect of the solute M elements on the activation energy for crystallization was evaluated from the exothermic peak temperature on the DSC curve by the Kissinger method [17]. As shown in Fig. 4, a linear relationship exists between $\ln(\Phi/T_p^2)$ and $1/T_p$, where Φ is the heating rate and T_p the peak temperature on the exothermic curve. The activation energy for crystallization estimated from the slope of these straight lines is plotted as a function of solute element concentration in Fig. 5. The energy is about 205 kJ mol^{-1} for $Zr_{85}Si_{15}$ and increases significantly by the replacement of zirconium with M elements. Although the replacement by all the solute elements results in an increase, the effectiveness is particularly large in the case of b c c elements vanadium, niobium and tantalum. Surprisingly, one can see that the activation energy increases even by the addition of nickel which resulted in a lowering of T_x. Even though the activation energy for crystallization evaluated by the Kissinger method includes both the energies for nucleation and growth of the crystalline phase, it can be confidently stated that the presence of multiple constituent elements in Zr–Si-based amorphous alloys results in a decreased growth of the crystalline phase through a lowering in the diffusivity of their elements.

Fig. 6 shows the variation of Vickers hardness values, H_v, of the ternary alloys as a function of the solute metal content. It is again interesting to note that the additions of group V and VI elements (Ta, Nb, V, Cr, Mo, W) having the b c c structure result in very high hardness values. While copper and nickel have negligible effect on H_v, both

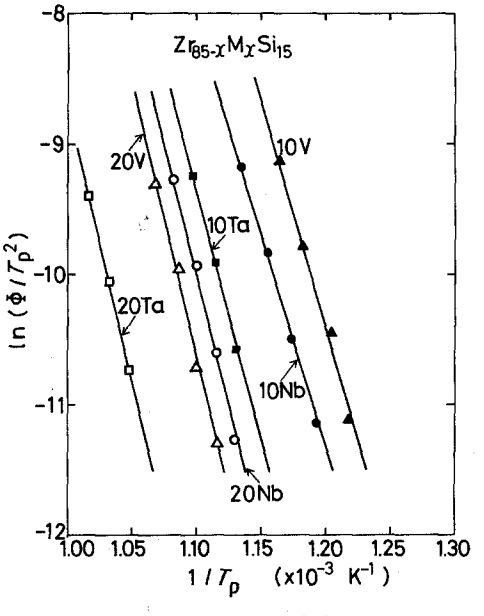

Figure 4 Kissinger plots of $\ln(\Phi/T_p^2)$ against $1/T_p$ for $Zr_{85-x}M_xSi_{15}$ (M = V, Nb or Ta) amorphous alloys. Φ is the heating rate and T_p is the exothermic peak temperature.

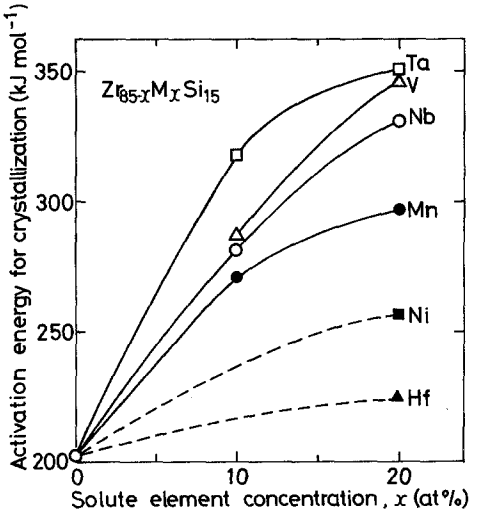

Figure 5 Change in the activation energy for crystallization of $Zr_{85-x}M_xSi_{15}$ ternary amorphous alloys with solute content (M = Hf, V, Nb, Ta, Mn or Ni).

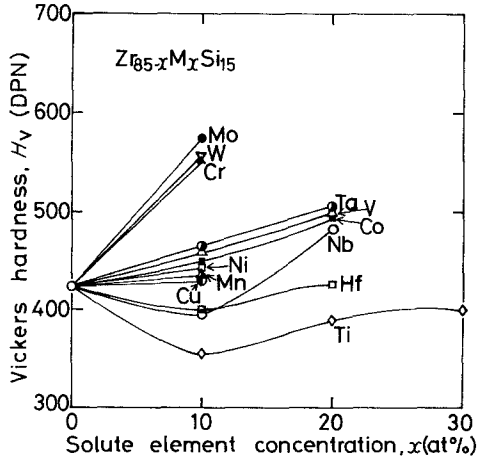

Figure 6 Change in the Vickers hardness (H_v) of $Zr_{85-x}M_xSi_{15}$ ternary amorphous alloys with solute concentration.

titanium and hafnium seem to lower the hardness of $Zr_{85}Si_{15}$ alloy.

Considering the variation of T_x and H_v with solute concentration, it becomes apparent that the b c c elements have a marked influence in increasing both H_v and T_x. On the other hand, the two homologous elements titanium and hafnium, which form isomorphous systems with zirconium under equilibrium conditions, decrease both H_v and T_x contrary to the expectation of solid-solution hardening. Thus, it may well be that the hardening phenomenon in amorphous alloys is quite different from the conventional crystalline alloys.

3.3. Crystallization behaviour

In this section, we present the results on the crystallization behaviour of $Zr_{85}Si_{15}$ and $Zr_{85-x}Nb_xSi_{15}$ amorphous alloys. The ternary alloy was chosen with the expectation that the phase crystallizing from the amorphous state may exhibit good superconducting properties. The general features of the exothermic peak in the DSC curves for these amorphous alloys are shown in Figs 7 and 8. The appearance of only one peak indicates that the transformation from the amorphous to the crystalline state occurs rapidly in a narrow temperature range, implying the simultaneous precipitation of crystalline phases. Furthermore, one can see that there is no significant change in the shape of the exothermic peak with silicon or niobium content.

In order to clarify in more detail the transformation from the amorphous to the crystalline phases, electron microscopic observations of structural changes in annealed $Zr_{85}Si_{15}$ and

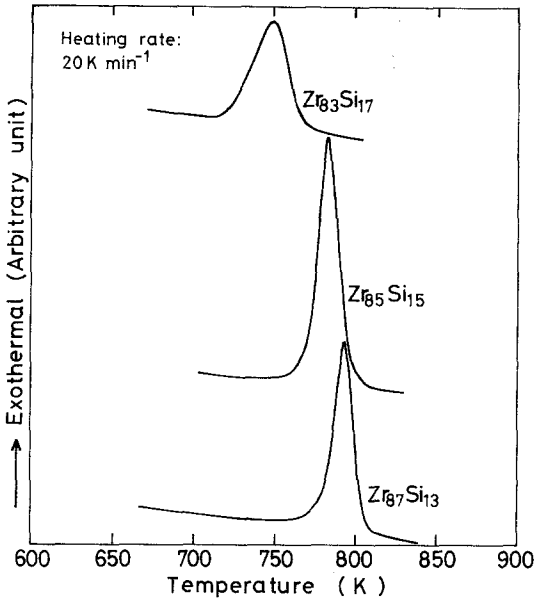

Figure 7 Differential scanning calorimetric curves of $Zr_{87}Si_{13}$, $Zr_{85}Si_{15}$ and $Zr_{83}Si_{17}$ amorphous alloys.

$Zr_{65}Nb_{20}Si_{15}$ amorphous alloys were carried out. In the $Zr_{85}Si_{15}$ alloy annealed for 0.5 h at 698 K, fine elliptical precipitates (about 80 nm x 20 nm) are seen over the entire area of the specimen (Fig. 9a). The diffraction pattern (Fig. 9b) indicates that this phase, co-existing with the amorphous phase, has a b c c structure with $a \simeq 0.35$ nm and corresponds to the β-Zr phase. Annealing at higher

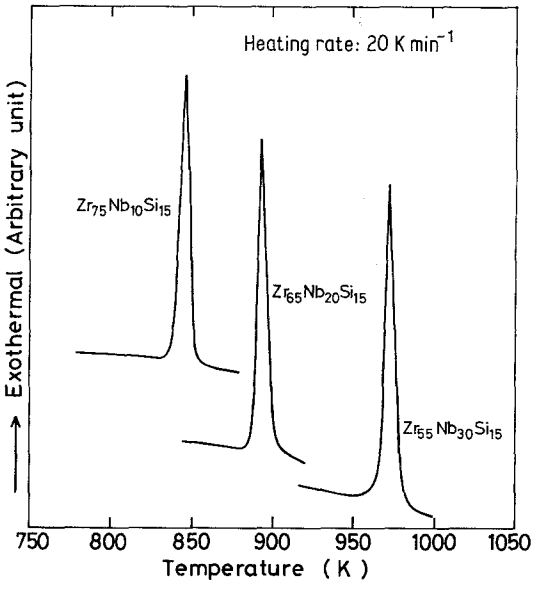

Figure 8 Differential scanning calorimetric curves of $Zr_{75}Nb_{10}Si_{15}$, $Zr_{65}Nb_{20}Si_{15}$ and $Zr_{55}Nb_{30}Si_{15}$ amorphous alloys.

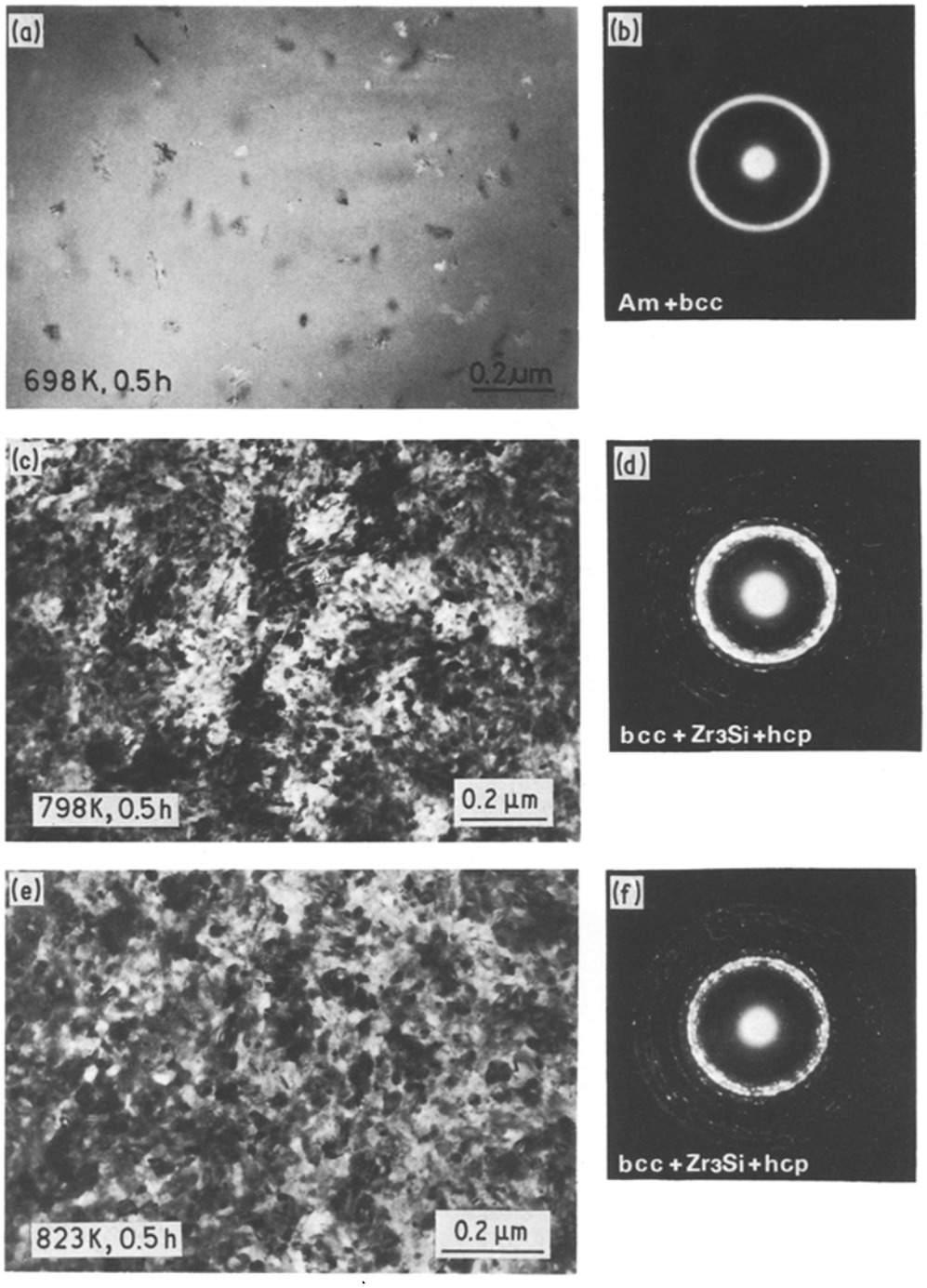

Figure 9 Transmission electron micrographs and selected-area diffraction patterns showing the progress of crystallization during annealing of $Zr_{85}Si_{15}$ amorphous alloys.

temperatures (798 K) results in the conversion of the majority of the remaining amorphous phase into a mixture of phases consisting of b c c β-Zr, h c p α-Zr and b c tetragonal Zr_3Si compound with $a \simeq 1.10$ nm and $c \simeq 0.55$ nm as shown in Fig. 9c and d. Judging from the results [18] that the equilibrium structure of $Zr_{85}Si_{15}$ alloy consists of α-Zr and Zr_4Si compound, it is concluded that the β-Zr and Zr_3Si precipitates exist in a non-equilibrium state. These phases remained unchanged even after annealing for 0.5 h at 823 K, as shown in Fig. 9e and f. However, much longer annealing treatments

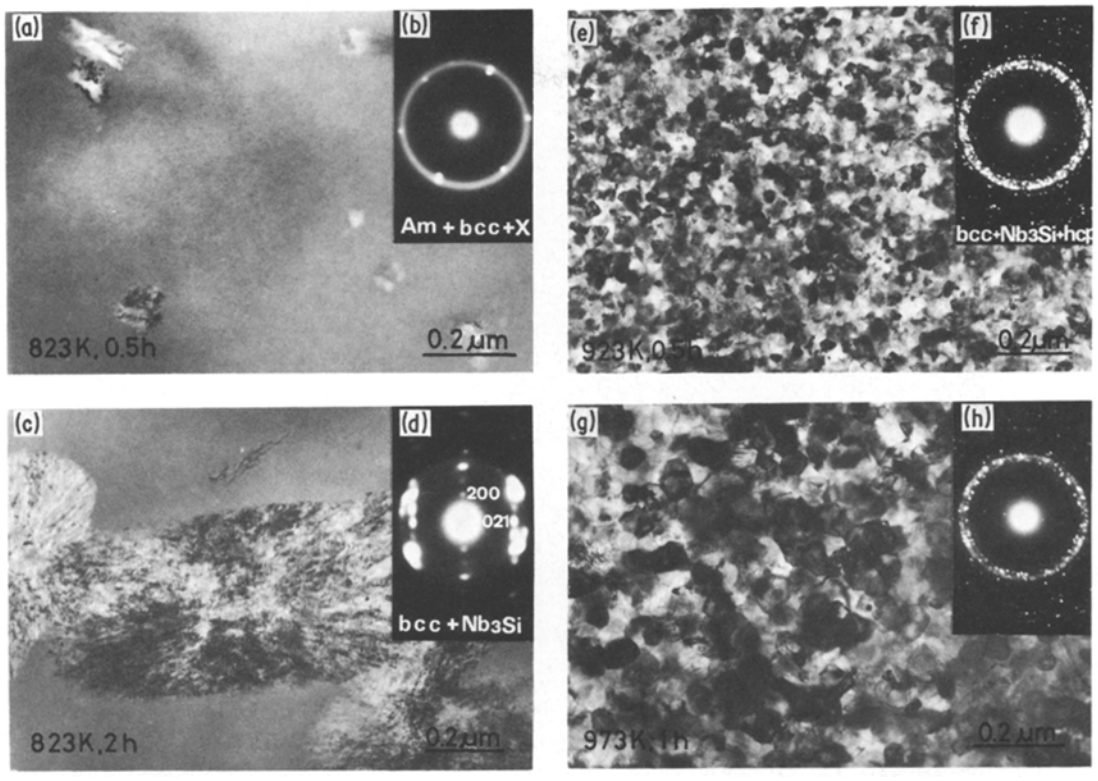

Figure 10 Transmission electron micrographs and selected-area diffraction patterns showing the annealed structures of $Zr_{65}Nb_{20}Si_{15}$ amorphous alloy.

resulted in the formation of α-Zr at the expense of β-Zr.

The crystallization process of $Zr_{65}Nb_{20}Si_{15}$ alloy is slightly different from that of $Zr_{85}Si_{15}$. When the specimen was annealed at 823 K, the aggregates consisting of β-Zr(Nb) and b c tetragonal Nb_3Si with $a \simeq 1.02$ nm and $c \simeq 0.52$ nm [19] nucleate and grow rapidly in the amorphous matrix, as shown in Fig. 10a to d. The devitrification of this alloy is rapid and on annealing at slightly higher temperatures the alloy seems to be completely converted into β-Zr and Nb_3Si. Subsequent annealing results in the formation of equilibrium phases α-Zr and Nb_3Si as shown in Fig. 10e and f, with a small quantity of β-Zr still remaining.

In the case of eutectic crystallization consisting of β-Zr(Nb) and Nb_3Si shown in Fig. 10e, it is seen that both the phases nucleate and grow maintaining a close orientation relationship between them. Several electron diffraction patterns showing mixed patterns of β-Zr(Nb) and Nb_3Si as represented in Fig. 11 were used to determine the orientation relationships. The following relationships were obtained, allowing for the maximum scattering within about 5°:

$$(1\,1\,1)_\beta \parallel (0\,1\,0)_{Nb_3Si}$$

$$(1\,\bar{1}\,0)_\beta \parallel (0\,0\,1)_{Nb_3Si}$$

$$(1\,1\,\bar{2})_\beta \parallel (1\,0\,0)_{Nb_3Si}.$$

On the basis of the orientation relationships determined in the present investigation, the amounts of lattice misfit between the two phases were calculated. The misfit of the lattices is about 2.3% for $(1\,1\,1)_\beta \parallel (0\,5\,0)_{Nb_3Si}$, 1.4% for $(1\,1\,0)_\beta \parallel (0\,0\,2)_{Nb_3Si}$ and 1.3% for $(1\,1\,2)_\beta \parallel (7\,0\,0)_{Nb_3Si}$. These small degrees of misfit indicate that the orientation relationship between β-Zr(Nb) and Nb_3Si are reasonably maintained in the crystallization reaction.

From the above result, the crystallization process in $Zr_{85}Si_{15}$ and $Zr_{65}Nb_{20}Si_{15}$ alloys appears to follow the sequence:

(1) $Zr_{85}Si_{15}$ alloy,

Amorphous → Am′ + β-Zr → β-Zr + Zr_3Si → β-Zr + α-Zr + Zr_3Si → α-Zr + Zr_3Si

(β-Zr: b c c, $a \simeq 0.35$ nm;
α-Zr: h c p, $a \simeq 0.32$ nm, $c \simeq 0.52$ nm;
Zr_3Si: b c tetragonal, $a \simeq 1.10$ nm,
$c \simeq 0.55$ nm;)

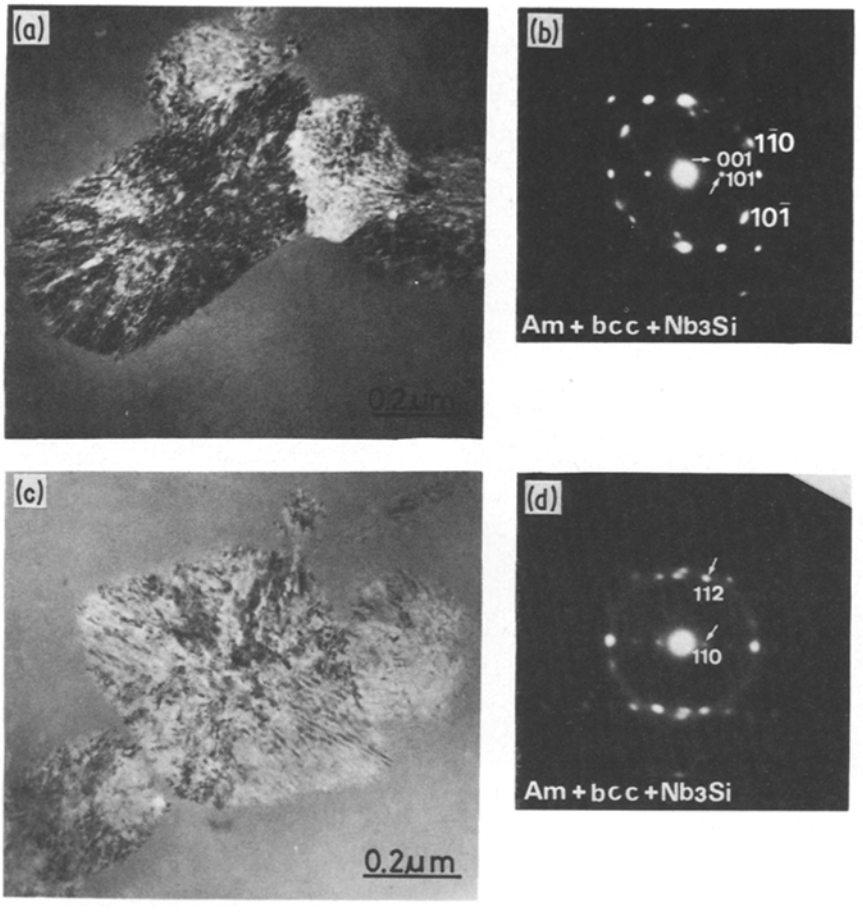

Figure 11 Transmission electron micrographs and selected-area diffraction patterns of $Zr_{65}Nb_{20}Si_{15}$ amorphous alloys annealed for 2 h at 823 K.

(2) $Zr_{65}Nb_{20}Si_{15}$ alloy,
Amorphous → β-Zr(Nb) + Nb_3Si →
β-Zr(Nb) + α-Zr(Nb) + Nb_3Si → α-Zr(Nb) + $(Nb, Zr)_3Si$

$$\left(\begin{array}{l}\beta\text{-Zr(Nb): b c c, } a \simeq 0.35\,\text{nm;}\\ \alpha\text{-Zr: h c p, } a \simeq 0.32\,\text{nm, } c \simeq 0.52\,\text{nm,}\\ Nb_3Si\text{: b c tetragonal, } a \simeq 1.02\,\text{nm,}\\ c \simeq 0.52\,\text{nm.}\end{array}\right)$$

4. Discussion

4.1. The effect of solute elements on T_x, ΔE and H_v

In a previous section, we showed that the replacement of zirconium by group V and VI elements (V, Nb, Ta, Cr, Mo, W) results in a significant increase in the crystallization temperature, the activation energy for crystallization and hardness and the effectiveness of other group IV, VII and VIII elements is much lower. Judging from the result that the effectiveness of the solute M elements on their properties can be clearly divided according to the group number of the periodic table, it seems that chemical bonding through the valence electrons is mainly responsible for such a compositional dependence. Furthermore, it is reasonably inferred that such changes in T_x, ΔE and H_v are due to the chemical bonding between the solute M element and silicon. The group V and VI elements which improve the properties significantly possess the common feature that half of the d-shell is vacant. Such an electronic configuration of these elements is favourable for the formation of strong chemical bonds with silicon, leading to higher values of T_x, ΔE and H_v. Titanium and hafnium also have a substantial number of empty d-states but show negligible effects as solutes on the properties of the Zr–Si amorphous alloys. This fact suggests that the electronic concentration in the d-shell of these elements is too low to form strong chemical bonds with silicon.

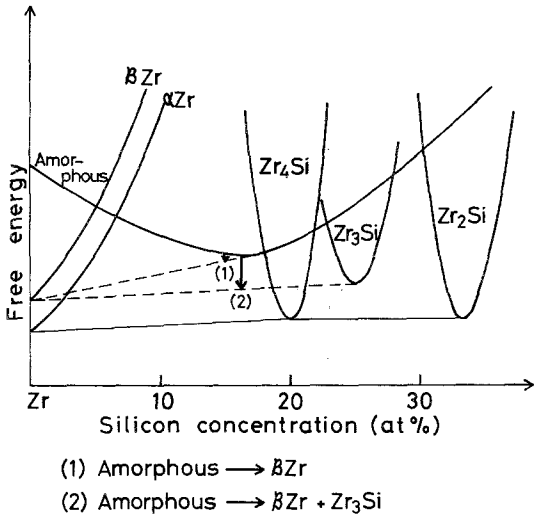

Figure 12 Hypothetical free energy diagram for the different phases in the Zr–Si system.

The atomic size effect appears to be less significant compared with the chemical bonding nature because the atomic size varies significantly even in the same group number.

4.2. Precipitation of metastable Zr_3Si compound

It should be emphasized that the Zr_3Si compound with a b c tetragonal structure is a metastable phase, since the first equilibrium intermediate phase co-existing with α-Zr is the Zr_4Si compound [18]. In this section, we shall discuss the reason why the Zr_3Si compound precipitated upon crystallization from the amorphous state. In order to understand the reactions which occur during crystallization of the $Zr_{85}S_{15}$ amorphous alloy, the hypothetical free-energy curves for the different stable and metastable phases are shown as a function of silicon concentration in Fig. 12. In the $Zr_{85}Si_{15}$ alloy, β-Zr phase precipitates by the primary crystallization process represented by Reaction 1. As a result, the remaining amorphous phase is enriched in silicon. Continued annealing results in the precipitation of β-Zr and Zr_3Si compound from the remaining amorphous phase enriched in silicon through Reaction 2.

Fig. 13 shows the electron diffraction patterns recorded from the $Zr_{85}Si_{15}$ (a) and $Zr_{65}Nb_{20}Si_{15}$ (b) alloys crystallized from the amorphous state. As can be seen clearly, the sequence, position and intensities of the Debye–Scherrer rings for the Zr_3Si compound agree very well with those from the Nb_3Si compound. This indicates that both the compounds have the same crystal structure and because of the slight change in the positions of the rings, the latter parameters may be slightly different. However, it appears that both Nb_3Si and Zr_3Si are isomorphous. Thus, it may in fact be that the tetragonal compound identified in the ternary alloy is $(Nb, Zr)_3Si$ instead of Nb_3Si. Hence, it is not surprizing that Zr_3Si compound precipitates during crystallization.

Another point of interest is that, as a general rule, the first intermediate phase to precipitate out from the amorphous alloy has a general formula A_3B–Fe_3B in Fe–B alloys [20, 21], Fe_3P in Fe–P alloys [22], Ni_3B in Ni–B alloys [23] and Ni_3P in

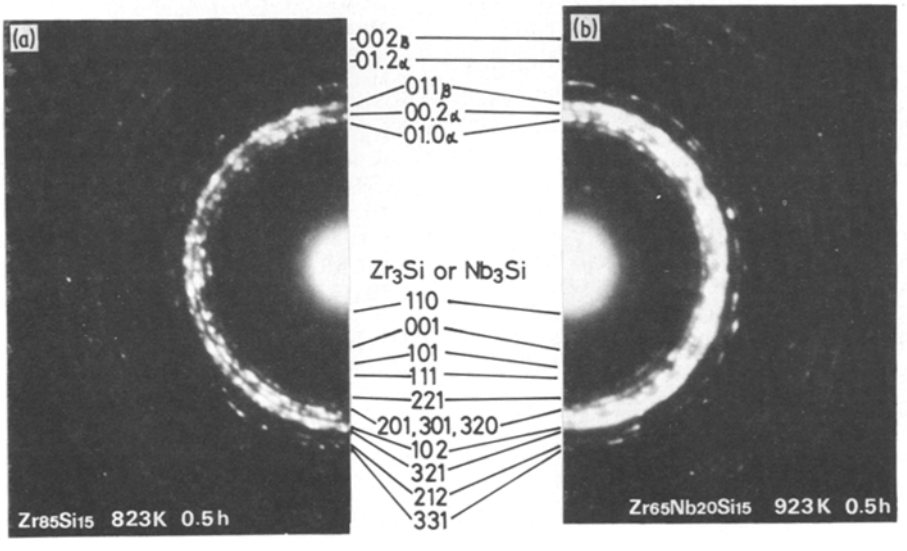

Figure 13 Electron diffraction patterns taken from the annealed structures of $Zr_{85}Si_{15}$ (a) and $Zr_{65}Nb_{20}Si_{15}$ (b) alloys.

Ni–P alloys [22]. All these compounds have a b c tetragonal structure, indicating that the precipitation of A_3B compounds may perhaps be favourable from the view points of free energy, atomic configuration, chemical bonding and others.

In the present investigation, we could not observe the formation of the equilibrium Zr_4Si phase even after annealing for 1 h at 1073 K, indicating that the metastable Zr_3Si compound is relatively "stable" against heating.

5. Conclusion

Amorphous single phases containing a large amount of M elements (M = Ti, Hf, V, Nb, Ta, Cr, Mo, W, Mn, Fe, Co, Ni or Cu) have been found in the $Zr_{85-x}M_xSi_{15}$ system. The solute element concentration in these amorphous alloys is in the range of 0 to 85 at% for titanium and hafnium, 0 to 80 at% Nb, 0 to 40 at% for vanadium and tantalum and 0 to 20 at% for chromium, molybdenum, tungsten, manganese, iron, cobalt, nickel and copper. All the amorphous alloys are so ductile that no crack is observed even after closely contacted bend tests. The crystallization temperature, activation energy for crystallization and hardness vary significantly by the replacement of zirconium with the solute M elements. In particular, the addition of the group V and VI elements results in a significant increase in their values. Such an increase could be explained by the assumption that a strong chemical bonding exists between the solute elements and silicon. The amorphous phase crystallizes following the process $Am \rightarrow Am' + \beta\text{-}Zr \rightarrow \beta\text{-}Zr + Zr_3Si \rightarrow \beta\text{-}Zr + \alpha\text{-}Zr + Zr_3Si$ for the $Zr_{85}Si_{15}$ alloy and $Am \rightarrow \beta\text{-}Zr(Nb) + Nb_3Si \rightarrow \beta\text{-}Zr(Nb) + Nb_3Si + \alpha\text{-}Zr$ for the $Zr_{65}Nb_{20}Si_{15}$ alloy. Among these crystalline phases, the Zr_3Si compound was found to be a metastable phase with a b c tetragonal structure.

References

1. C. SURYANARAYANA, "Structure and Properties of Amorphous Metals II", edited by T. Masumoto and T. Imura, *Supplement, Sci. Rep. Res. Inst. Tohoku Univ.* **A-28** (1980) 143.
2. H. S. CHEN, *Rep. Prog. Phys.* **43** (1980) 353.
3. C. SURYANARAYANA, "Rapidly Quenched Metals – A Bibliography 1973–1979" (IFI Plenum, New York, 1980).
4. A. INOUE, Y. TAKAHASHI and T. MASUMOTO, *Sci. Rep. Res. Inst. Tohoku Univ.* **A-29** (1981) 296.
5. N. TOYOTA, T. FUKASE, A. INOUE, Y. TAKAHASHI and T. MASUMOTO, *Physica* **107B** (1981) 465.
6. A. INOUE, Y. TAKAHASHI, N. TOYOTA, T. FUKASE and T. MASUMOTO, "Rapidly Quenched Metals IV" Vol. 2, edited by T. Masumoto and K. Suzuki (The Japanese Institute of Metals, Sendai, 1982) p. 1221.
7. K. H. J. BUSCHOW and N. M. BEEKMANS, *Phys. Rev. B* **19** (1979) 3843.
8. M. NOSE and T. MASUMOTO, *Sci. Rep. Res. Inst. Tohoku Univ.* **A-28** (1980) 232.
9. A. INOUE, H. M. KIMURA, S. SAKAI and T. MASUMOTO, "Titanium '80 – Science and Technology", Vol. 2, edited by H. Kimura and O. Izumi (The Metallurgical Society of AIME, Warrendale, 1980) p. 1137.
10. A. INOUE, Y. TAKAHASHI and T. MASUMOTO, unpublished research (1981).
11. M. H. COHEN and D. TURNBULL, *Nature* **189** (1961) 131.
12. D. TURNBULL, *Contemp. Phys.* **10** (1969) 473.
13. H. A. DAVIES, "Rapidly Quenched Metals III", Vol. 2, edited by B. Cantor (The Metals Society, London, 1978) p. 307.
14. M. NAKA, Y. NISHI and T. MASUMOTO, *ibid.*, Vol. 1, p. 231.
15. "Metals Handbook" 8th edn, Vol. 8, Metallography, Structures and Phase Diagrams (ASM, Metals Park, Ohio, 1973).
16. D. TURNBULL, *J. Phys. Colloque-4* **35** (1974) 1.
17. H. E. KISSINGER, *Anal. Chem.* **29** (1957) 1702.
18. C. E. LUNDIN, D. J. MCPHERSON and M. HANSEN, *Trans. ASM* **45** (1953) 901.
19. D. K. DEARDORFF, R. E. SIEMENS, P. A. ROMANS and R. A. MCCUNE, *J. Less-Common Metals* **18** (1969) 11.
20. U. HEROLD and U. KÖSTER, "Rapidly Quenched Metals III", Vol. 1, edited by B. Cantor (The Metals Society, London, 1978) p. 281.
21. J. L. WALTER and S. F. BARTRAM, *ibid.*, p. 307.
22. W. B. PEARSON, "A Handbook of Lattice Spacings and Structures of Metals and Alloys" (Pergamon Press, Oxford, 1967).
23. S. OHMORI, Y. HASHIMOTO, K. SHOJI, K. HIDAKA and Y. KODAIRA, *Powder Powder Metal.* **18** (1972) 316.

Received 22 February
and accepted 23 April 1982